



A SIMULATION STUDY ON THE EFFECT OF PARTICLE SIZE DISTRIBUTION ON THE PRINTED GEOMETRY IN SELECTIVE

Downloaded from: <https://research.chalmers.se>, 2026-06-15 20:27 UTC

Citation for the original published paper (version of record):

Ramesh Sagar, V., Lorin, S., Göhl, J. et al (2022). A SIMULATION STUDY ON THE EFFECT OF PARTICLE SIZE DISTRIBUTION ON THE PRINTED GEOMETRY IN SELECTIVE LASER MELTING. *Journal of Manufacturing Science and Engineering, Transactions of the ASME*, 144(5). <http://dx.doi.org/10.1115/1.4052705>

N.B. When citing this work, cite the original published paper.

Vaishak Ramesh Sagar¹

Department of Industrial and Materials Science,
Chalmers University of Technology,
Gothenburg SE-412 96, Sweden
e-mail: vaishak@chalmers.se

Samuel Lorin

Computational Engineering and Design
Fraunhofer Chalmers Centre,
Gothenburg SE-412 58, Sweden
e-mail: samuel.lorin@fcc.chalmers.se

Johan Göhl

Computational Engineering and Design
Fraunhofer Chalmers Centre,
Gothenburg SE-412 58, Sweden
e-mail: johan.gohl@fcc.chalmers.se

Johannes Quist

Computational Engineering and Design
Fraunhofer Chalmers Centre,
Gothenburg SE-412 58, Sweden
e-mail: johannes.quist@fcc.chalmers.se

Klas Jareteg

Computational Engineering and Design
Fraunhofer Chalmers Centre,
Gothenburg SE-412 58, Sweden
e-mail: klas.jareteg@fcc.chalmers.se

Christoffer Cromvik

Computational Engineering and Design
Fraunhofer Chalmers Centre,
Gothenburg SE-412 58, Sweden
e-mail: christoffer.cromvik@fcc.chalmers.se

Andreas Mark

Computational Engineering and Design
Fraunhofer Chalmers Centre,
Gothenburg SE-412 58, Sweden
e-mail: andreas.mark@fcc.chalmers.se

Fredrik Edelvik

Computational Engineering and Design
Fraunhofer Chalmers Centre,
Gothenburg SE-412 58, Sweden
e-mail: fredrik.edelvik@fcc.chalmers.se

Kristina Wärmefjord

Department of Industrial and Materials Science,
Chalmers University of Technology,
Gothenburg SE-412 96, Sweden
e-mail: kristina.warmefjord@chalmers.se

Rikard Söderberg

Department of Industrial and Materials Science,
Chalmers University of Technology,
Gothenburg SE-412 96, Sweden
e-mail: rikard.soderberg@chalmers.se

A Simulation Study on the Effect of Particle Size Distribution on the Printed Geometry in Selective Laser Melting

Selective laser melting (SLM) process is a powder bed fusion additive manufacturing process that finds applications in aerospace and medical industries for its ability to produce complex geometry parts. As the raw material used is in the powder form, particle size distribution (PSD) is a significant characteristic that influences the build quality in turn affecting the functionality and esthetic aspects of the product. This article investigates the effect of PSD on the printed geometry for 316L stainless steel powder, where three coupled in-house simulation tools based on discrete element method (DEM), computational fluid dynamics (CFD), and structural mechanics are employed. DEM is used for simulating the powder bed distribution based on the different powder PSD. The CFD is used as a virtual testbed to determine thermal parameters such as heat capacity and thermal conductivity of the powder bed viewed as a continuum. The values found as a stochastic function of the powder distribution are used to analyze the effect on the melted zone and deformation using structural mechanics. Results showed that mean particle size and PSD had a significant effect on the packing density, melt pool layer thickness, and the final layer thickness after deformation. Specifically, a narrow particle size distribution with smaller mean particle size and standard deviation produced solidified final layer thickness closest to nominal layer thickness. The proposed simulation approach and the results will catalyze the development of geometry assurance strategies to minimize the effect of particle size distribution on the geometric quality of the printed part. [DOI: 10.1115/1.4052705]

Keywords: selective laser melting, particle size distribution, geometric variation, 316L stainless steel, multiphysics modeling

1 Introduction

Additive manufacturing (AM) is an emerging manufacturing technique that has had a large impact on the manufacturing industry

¹Corresponding author.

Manuscript received December 30, 2020; final manuscript received October 1, 2021; published online October 25, 2021. Assoc. Editor: Tugrul Ozel.

thus far. This process has several advantages in comparison to traditional manufacturing techniques. For example, the part geometry is much freer, and there is no costly tool building required. Laser powder bed fusion technique such as the SLM process enable efficient utilization of the powder as the un-used powder can be recycled and reused. As the process consists of melting the raw material in powder form, the powder material characteristics are of prime importance in achieving the desired geometric quality. Particle size distribution (PSD) of the powder material is an important characteristic as it affects the final part properties [1].

Numerous research works on the influence of particle size distribution have been carried out. In Ref. [2], the effect of variation in PSD of Ti6Al4V powder on the microstructure and tensile strength was examined by comparing powders from three different suppliers. No significant differences in tensile strength and microstructure were found, but serious porosity issues were observed. Similar observations were made in a comparison study between fresh and recycled Ti6Al4V powder in terms of PSD and flow characteristics [3]. However, a study on the role of particle size on the tensile strength and dimensional accuracy in Refs. [4,5] showed that finer particle size resulted in higher tensile strength but lower dimensional accuracy along the Z-direction. In Ref. [6], the effect of spreading powders of different PSDs on the powder bed density was investigated. The study concluded that wide PSDs led to a higher powder bed density. The influence of uni-modal and bi-modal PSD on density, microstructure, and mechanical properties on 316 L [7] was examined by varying the energy density. The study revealed that the bi-modal powder had higher packing densities and greater layer thickness.

Similar advancements on the simulation front have been able to mimic various aspects of the SLM process to a larger extent. For example, transport phenomena for a single-track multilayer was simulated in Ref. [8] to predict the transient variation of the melt pool and solidified build geometry during deposition. The work in Ref. [9] simulated the influence of powder bulk density on the sensitivity of relative density of Ti6Al4V built parts. The work concluded that a decrease in bulk density adversely affected the relative density of the built parts. The influence of the particle size on the laser absorption was observed in Ref. [10] and laser absorptivity was found to decrease with an increase in the particle size. An optimization study for density control was performed in Ref. [11], and a prediction model was proposed. A numerical analysis was conducted in Ref. [12] to assess the powder bed generation and the single-track melting. The powder particle size was found to significantly contribute to the melt track distortion.

In summary of the aforementioned works, there exists thorough experimental investigation on the influence of PSD on the build's surface quality and the mechanical properties for various metal powders. However, knowledge of how the effect of PSD translates to the build's geometric accuracy is limited. Also, there is an increased interest toward integrating various simulation tools to capture such effects in the SLM process, especially to guide during the early product development stages. Hence, this forms the basis for the study conducted in this article.

1.1 Scope of This Article. In this article, the effect of PSD on the build geometry is examined by integrating various simulation tools that replicate the multiphysics aspects of the SLM process.

The design of experiment (DoE) approach is employed to investigate the effect of PSD on the build geometry. Three in-house simulation tools based on discrete element method (DEM), computational fluid dynamics (CFD), and structural mechanics are employed to generate the powder distribution, heat transfer, and displacement, respectively. A powder bed with a single layer consisting of two melt tracks is simulated in this article. However, learnings from this study will serve in setting up modeling and simulation to investigate multilayer multitrack builds. Packing density, powder layer thickness, melt pool layer thickness, layer displacement, and final layer thickness after dis-

placement are the responses measured from the simulations. The approach of combining three simulation tools establishes a way to calculate the effect of various aspects of the SLM process on the build geometry that could be used in scenarios that require detailed simulation accuracy.

This article is arranged as follows. Section 2 presents theoretical aspects of the SLM process, the concept of robust design, and background on the three in-house simulation tools. Experimental details at each step is described in Sec. 3. Section 4 presents the results and interpretation of the results. Section 5 concludes this article.

2 Theory

In this section, the theoretical background on the selective laser melting (SLM) process and the concept of robust design is given. Also, the principles of in-house built DEM, CFD, and structural mechanics-based simulations are described.

2.1 Selective Laser Melting. In the SLM process, the powder material is applied in the form of a layer on the build platform (Fig. 1). The laser source melts the powder and fuses the powder particles together. The powder is selectively melted in the layer as per a defined laser melt path (i.e., scan pattern), and the process is repeated layer by layer by lowering the build platform. The build platform is lowered as per the required layer thickness, and a roller or a recoater applies a new layer of powder material.

Once the build is complete, the build is removed from the build platform for further processing based on the end requirements.

In a powder bed fusion process, PSD is a powder characteristic that influences density, mechanical properties, and surface quality. PSD requires to be engineered to the specific AM process. For example, as the powder layer shrinks after melting and solidification, the thickness of the subsequent powder layer increases. For a smaller powder layer thickness, inappropriate PSD could cause porosity and affect the overall build quality [13].

2.2 Robust Design. Geometric variation occurs in every manufacturing process and the additive manufacturing process is no different. Variation in the manufacturing process parameters can cause inconsistencies between the design specifications (input) and the fabricated product (output). Reducing process variation to minimize its effect on the product's geometry is a complex and expensive approach. Instead, a cost-effective alternative would be to minimize the effect of process variation on the product's geometry. From a robust design perspective, the objective is to improve the quality of the product or the process by minimizing the effect of the causes of variation without eliminating the causes [14].

A product or a process is considered as a system as shown in the block diagram (Fig. 2). The response or the output of the system

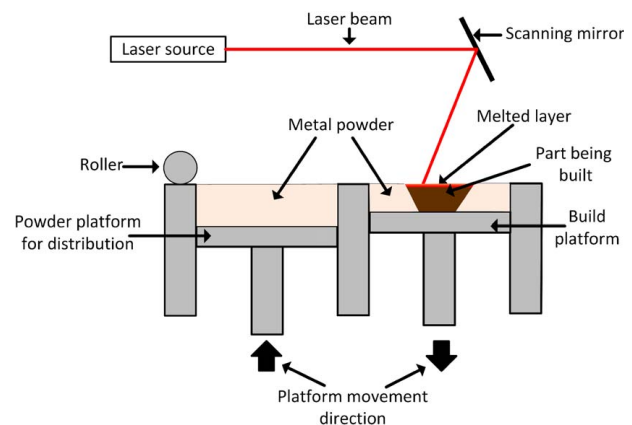


Fig. 1 Selective laser melting process

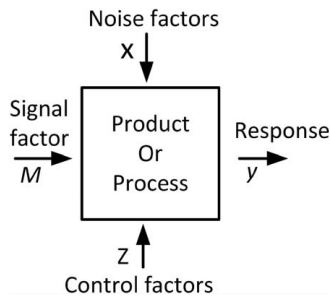


Fig. 2 P-diagram

denoted as y is the performance obtained. The system's performance is influenced by several factors. They are classified as signal factors (M), noise factors (x), and control factors (z). Signal factors represent the desired outcome from the system. Noise factors are uncontrollable parameters that cause variation in the system's response. Noise factors affecting the system's response could be some external factors such as operating environment, wear on usage, or internal factors such as system imprecision causing variation in system's response (unit-unit). Control factors are the parameters that could be adjusted to minimize the influence of noise factors and achieve the desired outcome.

To minimize the effect of variation in the SLM process, identifying the sources of variation and understanding their influence on the build geometry is necessary. In the context of this article, the stochastic powder distribution is treated as a variation source and its influence on the printed geometry is examined.

As a part is built layer by layer, the layer height or layer thickness is of interest, see Fig. 3. The stochastic powder distribution is viewed as a noise factor that could affect the intended nominal layer thickness. Here, the PSD is viewed as a control factor. From this perspective, the PSD could be engineered or optimized such that there is least variation between the nominal layer thickness and the printed layer thickness, or least variation among the printed layers.

2.3 Discrete Element Model. The DEM is used for simulating large populations of particles such as powders, granules, rock and ore particles, and many other materials. The DEM was originally proposed by Cundall and Strack in a series of publications [15] and has since been further developed by a wide range of contributors spanning many different fields of engineering and science. DEM is a numerical method based on Newtonian interactions of a system of particles where constitutive relations including contacts and collisions, heat transfer, inter-particle bonds, and forces and reaction to external fields are resolved. The DEM simulations in this article are performed in the DEM SOLVER DEMIFY™ developed at the Fraunhofer-Chalmers Centre (FCC). DEMIFY™ is a state-of-the-art DEM solver built to utilize the advantage of the

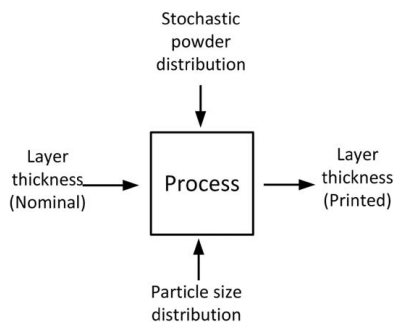


Fig. 3 Problem representation in the form of P-diagram with stochastic powder distribution as the noise factor and particle size distribution configuration as the control factor

parallel processing power of graphics processing units using the compute unified device architecture parallel computing platform.

2.4 Computational Fluid Dynamics. A computational fluid dynamics software, IPS IBOFLOW, is used to simulate the melt pool dynamics of the SLM process. IPS IBOFLOW developed at FCC is a finite volume-based solver for incompressible multiphase flow, which previously has been used to simulate, for example, additive manufacturing in bio printing [16] and surface tension driven flows [17].

Navier–Stokes equations, the transport equation for temperature together with the equation of the volume fraction advection are solved each time-step. The equations are discretized on a Cartesian octree grid, which can be dynamically refined and coarsened to enhance or reduce the resolution of the flow if necessary. This is convenient in flows that require a refined mesh at local areas, such as the interface between metal and gas.

The laser is modeled using a ray tracing algorithm, where the circular pattern of rays based on the laser diameter are directed from a moving laser source on the powder bed. The viscosity of the fluid metal is allowed to decrease with the increasing temperature, which is modeled with the Arrhenius equation. The specific heat capacity of the metal is based on the phase. The phase change is accounted for by adding the enthalpy of fusion to the specific heat capacity over the temperature interval between the solidus temperature and the liquidus temperature. To account for possible boiling, the enthalpy of vaporization is added to the specific heat capacity after the boiling point. The surface tension model used is temperature dependent and therefore has a tangential component to be able to model the Marangoni flow.

2.5 Structural Mechanics. The finite element method (FEM) is used to simulate how the solidified material distorts as well as to predict how the resulting strain and stress fields evolve as a result of the temperature and melting and solidification. The FEM approach for thermomechanical simulation of the AM process stems from welding simulation due to many similarities between welding and metal additive manufacturing simulations [18].

In this article, structural mechanics solver developed at FCC is used to perform the thermomechanical simulations. The material model is an elastoplastic with temperature-dependent material parameters. The constitutive model is based on infinitesimal strain theory, and the melted material is modeled using the silent approach, meaning that the material points that are not solid are given a compliant material property to not interfere with the solid part of the geometry while ensuring that the finite element mesh is intact and not too deformed, see Ref. [18]. This is done by setting Young's modulus to the value at the liquidation temperature for air and liquid metal.

Structural mechanics simulation captures how the powder melts, how the melt pool develops, how the pool is solidified, and how the shrinkage occurs.

3 Simulation Setup

In this section, details of the powder material and input parameters at each simulation stage are explained. Figure 4 illustrates the sequence of steps followed as well as the interaction of the simulation tools in this experimental setup.

The DEM simulations are first run to generate powder bed configurations for the chosen particle size distribution. The powder bed configurations along with the powder material properties and process parameters serve as input to the CFD simulations. The outcome of CFD simulations with information of powder bed with the solid/liquid status assists structural mechanics simulation to capture the process of melting, solidification, and deformation. The responses from each of these simulation stages are shown on the right side in Fig. 4.

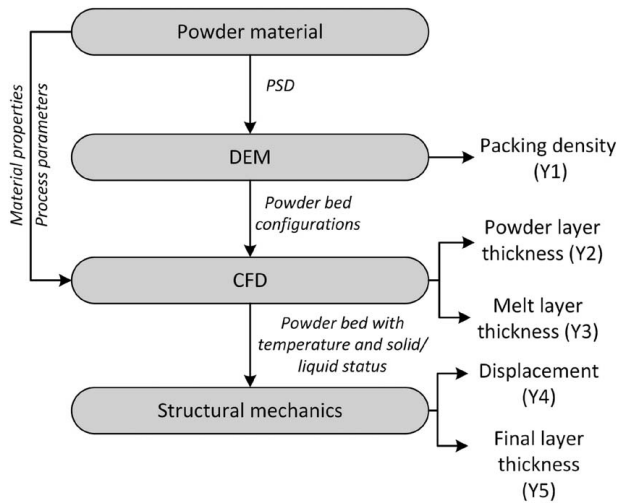


Fig. 4 Sequence of steps in the experimental setup

3.1 Powder Material. Powder of 316 L is used as the reference material. It is an austenitic stainless steel offering superior corrosion resistance and is a preferred material for elevated temperature-based applications. Table 1 provides the chemical composition [19]. Typical particle size distribution data from a powder manufacturer (GKN Hoeganaes, New Jersey, USA) has been used as the reference for generating a set of particle size distribution variants [19]. The characteristic sizes of the reference distribution are $x_{10}=16.3\ \mu\text{m}$, $x_{16}=21.0\ \mu\text{m}$, $x_{50}=34.6\ \mu\text{m}$, $x_{84}=47.9\ \mu\text{m}$, $x_{90}=50.9\ \mu\text{m}$, and $x_{99}=67.4\ \mu\text{m}$. The standard deviation of the distribution has been estimated to be $\sigma_{div}=13.5\ \mu\text{m}$. Here, the x_{10} and x_{90} values correspond to particle size diameter that accounts for 10% and 90% of the powder PSD, respectively. For simplicity, Gaussian normal distributions are used for generating the required distribution functions for the powder bed simulations in DEM.

3.2 Design of Experiments. The DoE method was opted in this study. Four input factors, namely, particle mean size, standard deviation, laser power, and hatch spacing were of interest. Laser scan speed and beam diameter were kept constant at 1000 mm/s and 0.05 mm, respectively. The nominal layer thickness was chosen to be $67.4\ \mu\text{m}$ (x_{99}). Table 2 provides details of the factors and their levels. A full factorial design was considered with four factors, each at two levels as specified in Table 2. The center points (reference points) were not considered in formulating the full factorial design. However, four runs at the center points were made for comparison.

Table 3 provides the details of the DoE configuration. The cumulative distribution and the frequency distribution of the particles for the simulation runs presented in Table 3 are shown in Fig. 5. For example, the dashed curve for the runs R9–12 in Fig. 5 represents the PSD configuration employed for the simulation runs R9–R12 (Table 3) along with the details of the mean particle size and the standard deviation values.

3.3 Discrete Element Method Case Configuration. Powder particles were generated in a domain above the intended bed and

Table 1 Chemical composition of 316 L (wt%)

Cr	Si	Mn	Ni	Mo	Fe	C	S	O	N
16.5	0.45	1.2	11	2.2	Bal	0.012	0.029	0.069	0.098

Table 2 Factors and their levels in the DoE configuration

Label	Factor	-1	0	+1
X1	Mean particle size, x_{50} (μm)	21.1	34.6	48.0
X2	Standard deviation, σ_{dev} (μm)	2.7	13.5	24.2
X3	Laser power, P (W)	100	150	200
X4	Hatch spacing, H_s (μm)	50	70	90

Table 3 DoE matrix

Runs	X1	X2	X3	X4	Runs	X1	X2	X3	X4
1	-1	-1	-1	-1	11	+1	-1	+1	-1
2	-1	-1	-1	+1	12	+1	-1	+1	+1
3	-1	-1	+1	-1	13	+1	+1	-1	-1
4	-1	-1	+1	+1	14	+1	+1	-1	+1
5	-1	+1	-1	-1	15	+1	+1	+1	-1
6	-1	+1	-1	+1	16	+1	+1	+1	+1
7	-1	+1	+1	-1	17	0	0	0	0
8	-1	+1	+1	+1	18	0	0	0	0
9	+1	-1	-1	-1	19	0	0	0	0
10	+1	-1	-1	+1	20	0	0	0	0

were allowed to free fall and settle (see Fig. 6). It must be noted that this configuration does not consider a recoater system for spreading the powder on the build platform. This is because the effect of a specific recoater (hard or soft) as a source of variation can be avoided.

Therefore, a free-fall approach was employed to generate the stochastic nature of the powder distribution. In the free-fall approach, the mass rate, insertion rate, generator domain volume, and target particle size distribution configuration are critical for the formation of the powder bed. The particles are instantiated at random positions in a generator domain with a specified mass rate. The insert frequency controls how often particles are generated. In this article, an insertion frequency of 100 Hz was used. The generator algorithm keeps track of the generated mass in each particle size class and controls for continuously maintaining the size distribution target. The total simulation time was 1 s where the particles were created from 0 to 0.5 s, and in the remaining 0.5 s, the particles were allowed to settle down and become still.

Material model parameters and simulation settings are provided in Table 4. The powder PSD is set according to a truncated normal distribution with mean and standard deviation values according to the DoE setup in Table 3. A general illustration of different powder packing configurations that could be generated is provided in Fig. 7.

3.4 Computational Fluid Dynamics. The parameter values for 316 L used in CFD simulation were obtained from Refs. [20,21] and are tabulated in Table 5. Same material (316 L) was chosen for the substrate as well. The size of computational domain was set to $1\ \text{mm} \times 0.3\ \text{mm} \times 0.4\ \text{mm}$ (Fig. 8). A continuous heat source model with Gaussian distribution was employed. As mentioned earlier, the intended beam diameter was 0.05 mm ($D4\sigma$). Two tracks were melted with each track length measuring 0.8 mm. The computational mesh was dynamically refined to enhance the resolution of the metal surface, parameter value unit where the finest mesh size used was $6.25\ \mu\text{m}$. A constant time-step density (ρ) of $7269\ \text{kg/m}^3$ of $0.1\ \mu\text{s}$ was used in simulations. Figure 9 illustrates the CFD simulation of the melt pool.

3.5 Structural Mechanics. The temperature and solid/liquid status of the material at different points are extracted from CFD simulation to calculate the stress and strain fields and the resulting

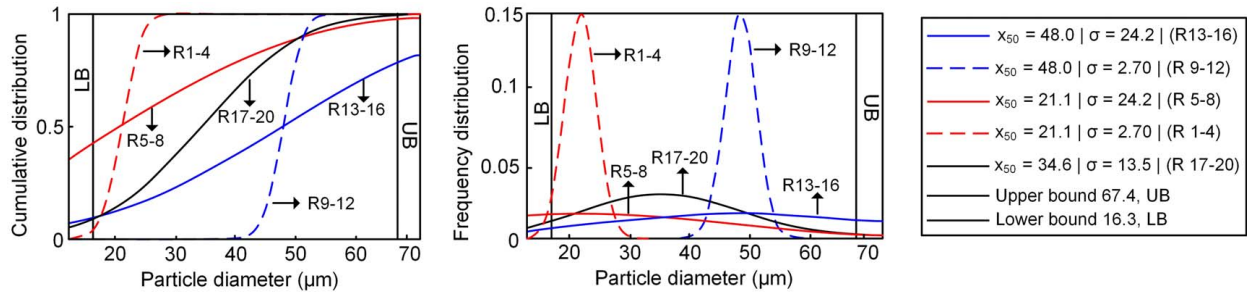


Fig. 5 Powder particle size distributions simulated as per the DoE configuration. Cumulative distribution (left), frequency distribution (center) and respective labelling and legend details (right).

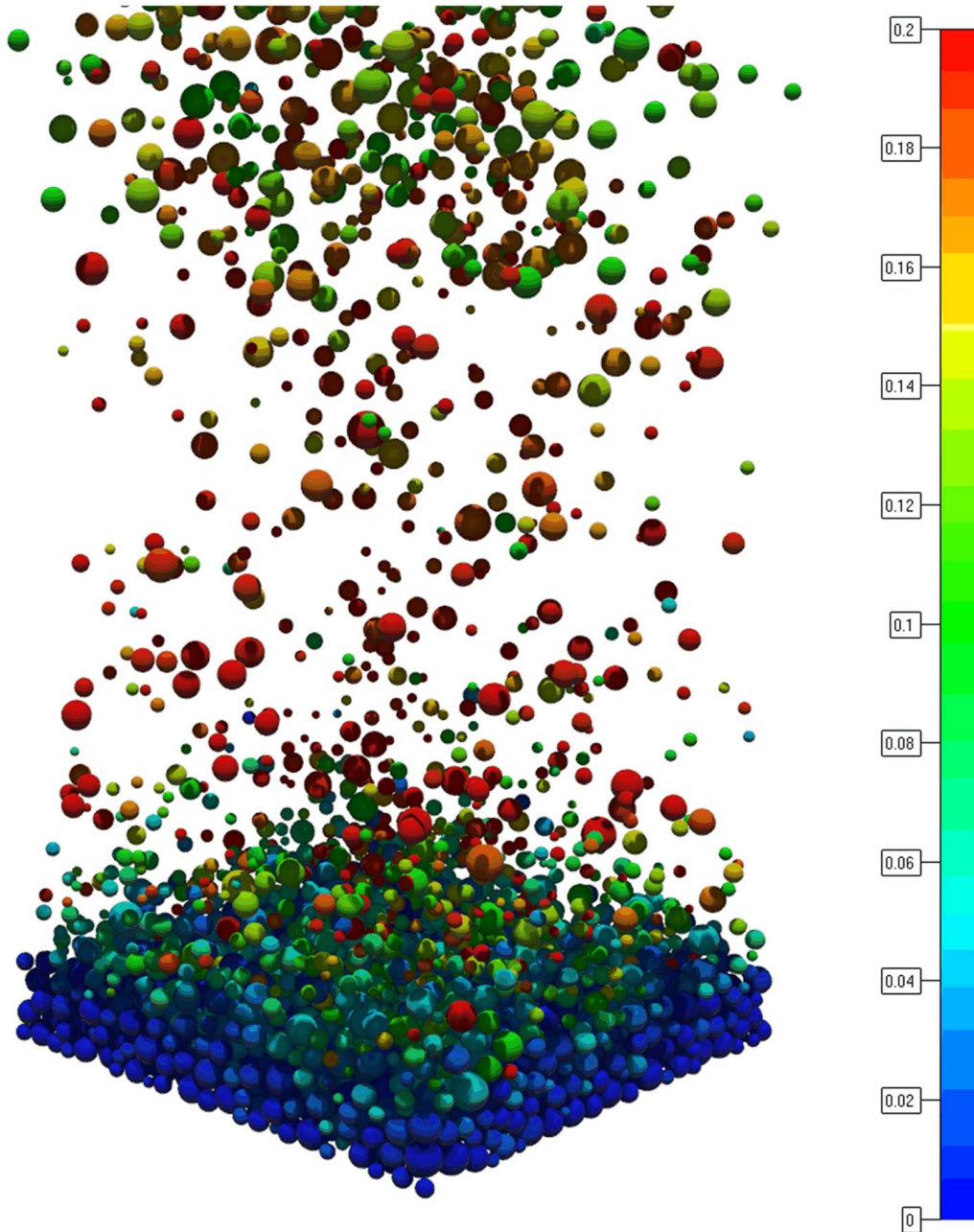


Fig. 6 Snapshot of the filling procedure of the particle bed formation. Particles colored by velocity (color map unit in m/s).

Table 4 Parameters used in the DEM simulation

Parameter	Value	Unit
Solid density, ρ_s	7269	kg/m ³
Static friction p-p, μ_s	0.4	—
Static friction p-w, μ_s	0.4	—
Rolling friction p-p, μ_r	0.005	—
Rolling friction p-w, μ_r	0.005	—
Surface energy p-p, γ	0.1	mJ/m ²
Young's Modulus, E	200e6	Pa
Poisson's ratio, ν	0.294	—
Time-step, dt	8.7e-8	s
Particle insertion frequency	100	Hz

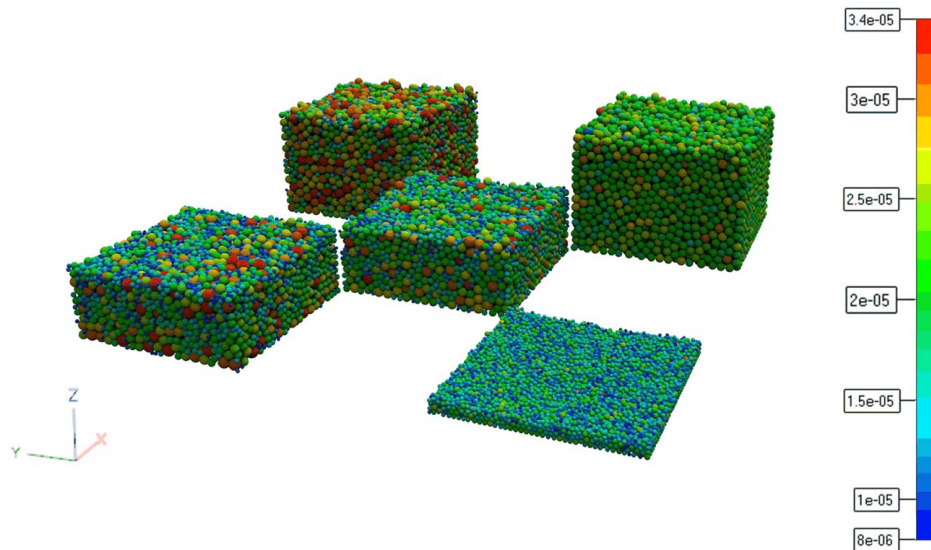


Fig. 7 Illustration of the five different powder particle packing configurations simulation. Particles colored by radius, unit in m.

displacement. The bottom of the base plate is locked from translation in z-direction, the point (0, 0, 0) is locked from translation in x- and y-direction, and finally, the point (1, 0, 0) is locked from translation in the x-direction.

In Fig. 10, the geometry is depicted when the laser has melted the track on the right side. Here, only the part of the computational model that is solid is shown. In a cross section, it is seen how the equivalent plastic strain (middle) and the von Mises stress (bottom) are growing as the structure is cooling down. These fields depend on how the geometry was melted.

Table 5 Parameters used in the CFD simulation

Parameter	Value	Unit
Density, ρ_s	7269	kg/m ³
Density, ρ_l	6881	kg/m ³
Viscosity, η	0.008	Pa s
Specific heat capacity, $C_{p(s)}$	688.6	J/(kg K)
Specific heat capacity, $C_{p(l)}$	773.7	J/(kg K)
Thermal conductivity, $k_{(s)}$	32.17	W/(m K)
Thermal conductivity, $k_{(l)}$	27.5	W/(m K)
Liquidus temperature, T_l	1723	K
Solidus temperature, T_s	1658	K
Enthalpy of fusion, ΔH_f	260	kJ/kg
Boiling point, T_b	3090	K
Enthalpy of vaporization, ΔH_v	7406	kJ/kg
Emissivity, ϵ	0.36	K
Surface tension, γ	1.76	N/m

4 Results and Discussion

In this section, the outcome from the DEM, CFD, and structural mechanics simulations are presented and discussed. Table 6 summarizes the results.

Packing density (Y1) was measured as the response from DEM simulations. From CFD simulations, the mean powder layer thickness before melting (Y2) and the mean melt pool layer thickness (Y3) were measured as responses. Figure 11 presents a sample result of the surface map (from R1) and plots showing the Y2 response. Figure 12 presents a sample visualization of layer height, surface temperature, and melt pool in CFD simulation. Layer displacement after shrinkage (Y4) and mean layer thickness after displacement (Y5) were captured from the structural mechanics simulations.

4.1 Discussion. The statistical analysis was performed to analyze the significance of the sources (X1–X4) on the responses

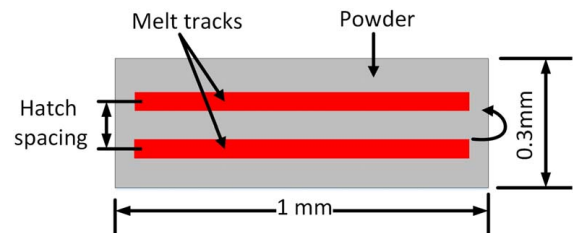


Fig. 8 Computational domain and the scanning strategy details

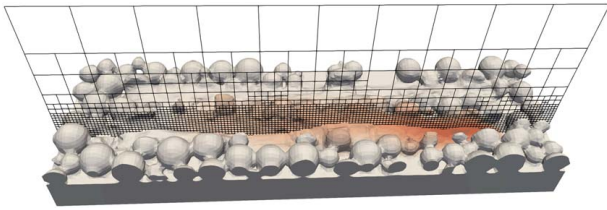


Fig. 9 A CFD simulation of the melt pool with a slice of the computational grid

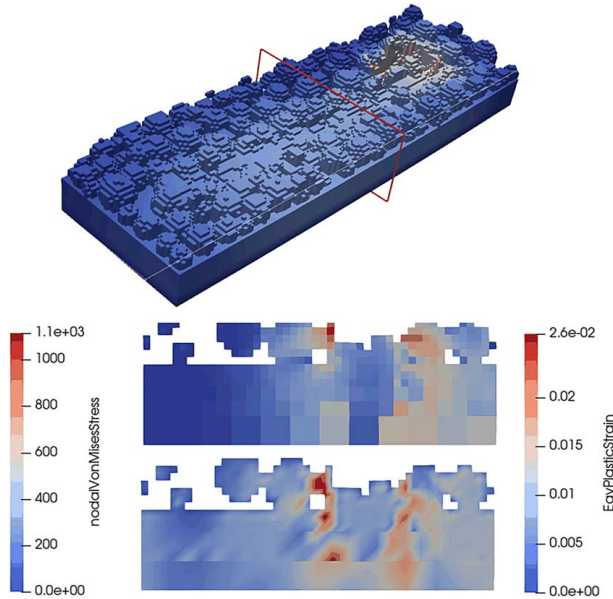


Fig. 10 A thermomechanical simulation coupled to the CFD simulation. A cross section of equivalent plastic strain (middle) and Von Mises stress (below)

(Y1–Y5), and the results are tabulated in Table 7. The significance of a source is assessed using the P-value, where a P-value of < 0.05 is considered significant.

From the DEM simulations, the response Y1 was analyzed with reference to the input sources, the mean particle size (X1), and

standard deviation (X2). Both X1 and X2 were found to be affecting the packing density. However, X1 was observed to have more significant effect on the packing density. Also, it could be observed from Table 6 that a wider particle size distribution lead to an increase in packing density, which was significantly smaller.

The response Y2 was analyzed with respect to input sources X1 and X2. No significant effect of X1 and X2 on the mean powder layer thickness (Y2) was observed from the statistical analysis based on the number of runs performed.

The response Y3 was analyzed with respect to X1, X2, laser power (X3), and hatch spacing (X4). From the analysis, it was observed that X1, X2, X3, and the interaction of X1 and X2 had significant effect on the melt pool layer thickness with X1 being the most significant. A PSD with smaller X1 and X2, i.e., a narrow PSD resulted in higher melt pool layer thickness. Also, for any given PSD, the melt pool layer thickness was found to decrease with an increase in laser power. Increasing the laser power can cause the neighboring particles along the track to melt, thereby causing a change in the layer thickness. From Table 6, it can be observed that Y3 increases with an increase in Y2.

The mean layer displacement (Y4) was analyzed in reference to all the input sources, X1–X4. Laser power (X3) was found to be the most significant of all, followed by hatch spacing (X4) and the interaction effect of X3 and X4. For any given PSD, higher X3 and lower X4 produced the maximum deformation.

The final mean layer thickness (Y5) was analyzed in reference to all the input sources as well. X1, X2, X3, and X4 were all found to have a significant effect on the final layer thickness. However, in terms of PSD, a narrow PSD with smaller mean particle size, X1, and smaller standard deviation resulted in a higher final mean layer thickness (R1–R4) that is nearest to the chosen nominal layer thickness value of $67.4 \mu\text{m}$ (x_{99}). In case of PSD with a larger mean particle size, X1 resulted in lower final mean layer thickness.

4.1.1 Effect of Particle Size Distribution on the Effective Powder Layer Thickness. The powder layer thickness of the subsequent layer also known as the effective powder layer thickness mainly depends on the layer thickness of the previously solidified layer and will be larger than the preset nominal thickness. Figure 13 demonstrates the effective powder layer thickness (T_{eff}) and final layer thickness (T_f) for the runs R1 and R9. The estimations are made with the help of final layer thickness (Y5) measured from structural mechanics simulations. For run R1, the final layer thickness (Y5) for the first layer was measured to be

Table 6 Design of experiments table and response measurement values, all units in microns

Runs	Powder bed	X1	X2	X3	X4	Y1	Y2	Y3	Y4	Y5
1	PB1	-1	-1	-1	-1	0.5522	53.1076	49.1498	5.0856	53.3759
2	PB1	-1	-1	-1	+1	0.5522	53.1076	49.5909	5.1383	53.1075
3	PB2	-1	-1	+1	-1	0.5521	53.7565	46.3849	14.7482	60.543
4	PB2	-1	-1	+1	+1	0.5521	53.7565	46.9136	11.35	57.3954
5	PB3	-1	+1	-1	-1	0.5651	43.9863	30.4398	5.8747	35.2372
6	PB3	-1	+1	-1	+1	0.5651	43.9863	32.009	5.3124	35.7481
7	PB4	-1	+1	+1	-1	0.5684	49.7114	29.2887	17.2088	45.4065
8	PB4	-1	+1	+1	+1	0.5684	49.7114	29.6487	12.7126	41.8453
9	PB5	+1	-1	-1	-1	0.5735	37.6448	28.5291	6.0085	33.6244
10	PB5	+1	-1	-1	+1	0.5735	37.6448	29.7874	5.8972	34.0807
11	PB6	+1	-1	+1	-1	0.5752	45.1844	24.774	18.096	42.108
12	PB6	+1	-1	+1	+1	0.5752	45.1844	25.0484	13.2268	37.9345
13	PB7	+1	+1	-1	-1	0.5838	42.2659	32.0396	5.7657	36.7493
14	PB7	+1	+1	-1	+1	0.5838	42.2659	32.5127	5.3705	36.4885
15	PB8	+1	+1	+1	-1	0.5862	51.5537	27.5715	17.1439	43.6121
16	PB8	+1	+1	+1	+1	0.5862	51.5537	27.679	12.9157	40.2364
17	PB9	0	0	0	0	0.5709	41.0798	29.5882	11.9276	41.1862
18	PB10	0	0	0	0	0.5767	39.5343	28.8132	12.5604	40.9652
19	PB11	0	0	0	0	0.5624	40.7313	29.2121	12.4783	41.2332
20	PB12	0	0	0	0	0.5700	40.0916	29.5908	12.0801	41.4156

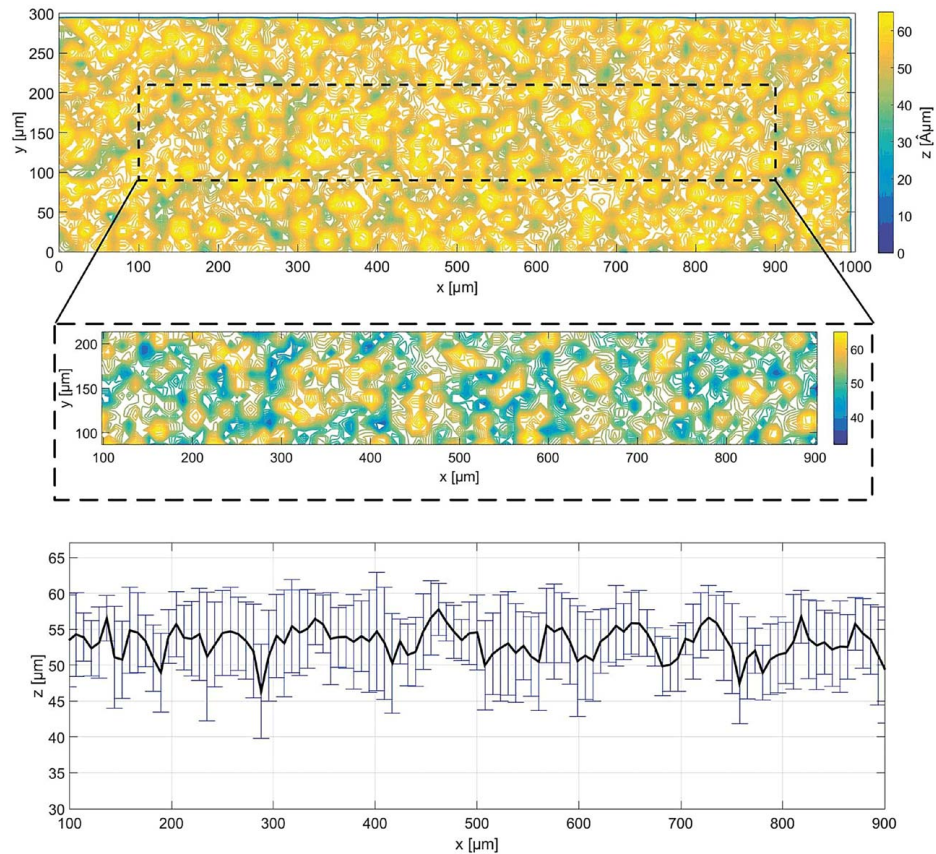


Fig. 11 From R1, (a) surface contour plot with magnified region highlighting the melted area and (b) mean layer thickness plot along the melt track

$53.38 \mu\text{m}$ and is approximately 79% of the nominal layer thickness of the first layer, $67.4 \mu\text{m}$. Therefore, lowering the build platform by nominal layer settings of $67.4 \mu\text{m}$ will cause the effective powder layer thickness of the second layer to be $81.42 \mu\text{m}$. Assuming the final layer thickness of each layer will be approximately 79% of their respective effective powder layer thickness, the final layer thickness is estimated to reach a stable value of $67.4 \mu\text{m}$ after building about seven layers. Similarly in R9, the final layer thickness, Y5 for the first layer was measured to be $33.62 \mu\text{m}$ and is approximately 50% of the nominal layer thickness of $67.4 \mu\text{m}$. The effective powder layer thickness of the second layer can be estimated to be $101.18 \mu\text{m}$. Assuming the final layer thickness of each layer will be approximately 50% of their respective effective powder layer thickness, the final layer thickness will reach a stable value of $67.4 \mu\text{m}$ after building about 13 layers.

Regardless of the PSD configuration in R1 and R9, the solidified final layer thickness stabilizes after initial set of layers. However, it is interesting to observe the differences between the effective powder layer thickness ($T_{e f p}$) and final layer thickness (T_f), which can be traced back to the PSD configuration, i.e., the mean particle size and the standard deviation.

The effect of layer thickness variation in the initial stages of the print could be negated by considering the support structures, which after the build would be cut off as also discussed in Ref. [22]. This, however, may affect the processing strategy adapted such as the orientation of the build geometry, the overall processing time required in the presence or absence of the support structures, and the number of layers required. Also, the variation in layer thickness may be considered negligible based on whether the geometric features in the build is macroscopic or microscopic in nature.

While the layer thickness stabilizes after a set of initial layers, the layer surface variation within the layer caused by the PSD as shown

in Fig. 11 may affect the powder distribution in the subsequent layers. This may get further aggravated due to the residual distortion.

4.1.2 Effect of Particle Size Distribution on Residual Stress State. The effect of hatch spacing and the PSD configuration in

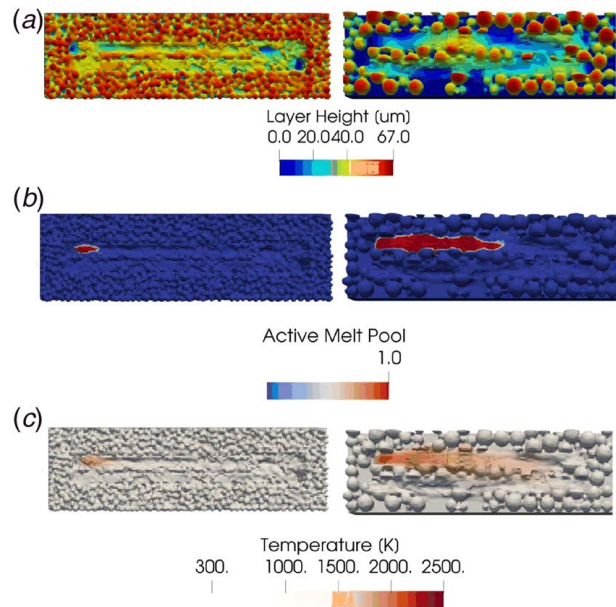
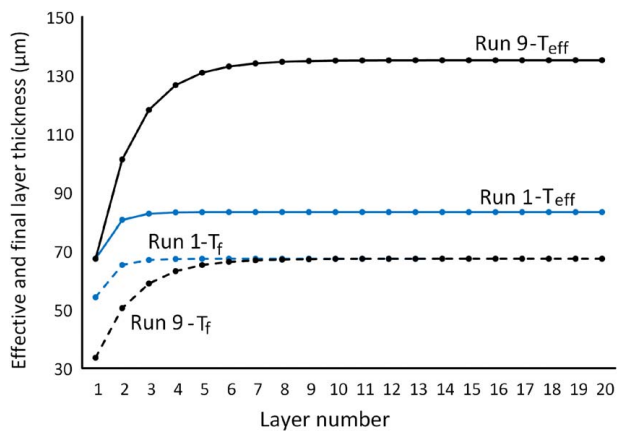
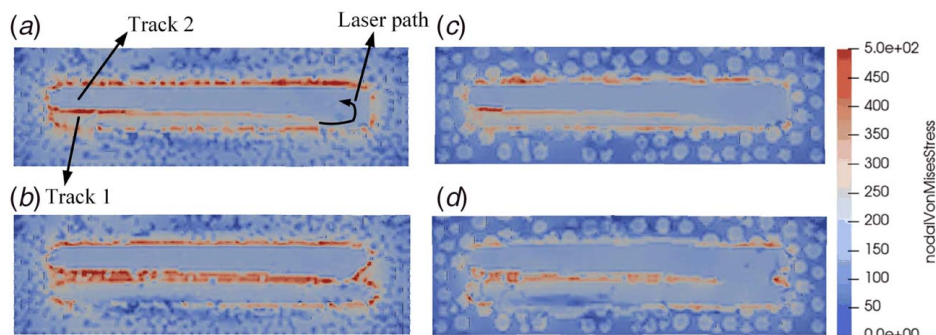


Fig. 12 Visualization of runs R1 and R16 as an example showing (a) layer height, (b) surface temperature, and (c) active melt pool from end of CFD simulations

Table 7 Statistical analysis on the effect of input sources and their significance on the responses

Y (response)	X (source)	F-ratio	P-value
Packing density (Y1)			
Y1	X1(21.1,48)	57.127	0.0001
Y1	X2(2.7,24.2)	22.279	0.0015
Y1	X1*X2	0.529	0.4878
Mean powder layer thickness (Y2)			
Y2	X1*X2	2.751	0.1358
Y2	X1(21.1,48)	2.711	0.1383
Y2	X2(2.7,24.2)	0.024	0.8805
Mean melt pool layer thickness (Y3)			
Y3	X1(21.1,48)	21.835	0.0000
Y3	X1*X2	57.665	0.0000
Y3	X2(2.7,24.2)	29.680	0.0004
Y3	X3(100,200)	6.0893	0.0357
Y3	X4(50,90)	0.214	0.6548
Mean layer deformation (Y4)			
Y4	X3(100,200)	185.025	0.0000
Y4	X4(50,90)	11.275	0.0084
Y4	X3*X4	8.874	0.0155
Y4	X1(21.1,48)	1.713	0.2230
Y4	X1*X2	1.617	0.2354
Final mean layer thickness (Y5)			
Y5	X1(21.1,48)	264.195	0.0000
Y5	X1*X2	248.666	0.0000
Y5	X2(2.7,24.2)	141.010	0.0000
Y5	X3(100,200)	111.931	0.0000
Y5	X3*X4	9.416	0.0134
Y5	X4(50,90)	8.327	0.0180

**Fig. 13 Effective powder layer thickness (T_{eff}) and final solidified layer thickness (T_f) estimated for runs R1 and R9****Fig. 14 Visualization of final stress state in the runs (a) R1, (b) R2, (c) R13, and (d) R14 as an example from structural simulations**

terms of particle size and standard deviation settings on the resulting stress state in the contact region of the melted tracks and the build platform is shown in Fig. 14. For example, in R1, owing to the smaller mean particle size and standard deviation settings in the PSD configuration and low hatch spacing settings, the two melt tracks fuse together with the fusion of powder particles more evident on the right side of the powder bed (as shown). This occurs because the laser heat source transits from the first track to the second track as per the scanning path. The distinctive gap of the track boundaries on the left side of the powder bed (as shown) could mean an unmelted zone, which is more clearly visible in R2. The higher hatch spacing in R2 results in a gap between the melted tracks and leads to partial melting or unmelted powder particles and porosity.

Contrary to runs R1 and R2, the runs R13 and R14 have a wider PSD configuration in terms of mean particle size and standard deviation settings. The effect of such a configuration is evident in the color mapping of the stress state along the boundaries of the melted zone and the track boundaries. Larger mean particle size with lower power settings and higher hatch spacing settings cause partial melting of the powder particles between the melting tracks as clearly shown in Figs. 12 and 14.

It is also important to note from the earlier discussed observations that the different PSD configurations and hatch spacing settings also affects the melt track width. This is due to the nature of powder distribution, which influences the powder availability along the melt track. Variation in powder availability can lead to inconsistent melt track widths and cause remelting of already solidified melt tracks or the layers beneath, thereby influencing the residual stress state and deformation. The magnitude of residual stresses could vary in a multilayer, multitrack build, which in turn could affect the geometric dimensions after the build is cut off from the build platform.

5 Conclusion and Future Work

Additive manufacturing of metals is being vastly adapted within various industries. Utilizing its potential to the fullest requires understanding of various factors in the process that contribute to the build quality. Influence of metal powder characteristics such as the particle size distribution is one such factor that requires to be well understood. With this being the objective, the effect of PSD on the printed geometry was examined in this article.

The robust design method was employed where the stochastic powder distribution on the powder bed was treated as the noise factor and the PSD configuration was treated as the control factor. Their influence on the printed geometry in the form of layer thickness was observed. To perform this study, a simulation method was presented by integrating DEM, CFD, and structural mechanics-based simulation platforms. Packing density, powder layer thickness, melt pool layer thickness, layer displacement, and finally, the solidified layer thickness were measured as responses from the simulation study.

For the chosen nominal layer thickness (67.4 μm), it was seen that the mean particle size greatly influenced the layer thickness. Specifically, a PSD configuration with smaller mean particle size and smaller standard deviation settings produced results closest to the preset nominal layer thickness. Also, it was observed that the particle size distribution configuration influenced the powder availability, variation in the melt track width, and the resulting stress buildup at the melted area and build platform interface.

These observations can support in engineering the PSD that is suitable for the chosen nominal layer thickness. Another option would be to test a lower nominal layer thickness value for the same PSD configurations considered in this study. But a lower nominal layer thickness will increase the build processing time. Hence, there will be a trade-off between the choice of nominal layer thickness and the build processing time.

On the basis of the aforementioned findings, the prospect of the proposed simulation method of integrating simulation tools to investigate various aspects of the powder bed fusion process (SLM) was found to be promising. The presented simulation approach can serve in analyzing the process windows that accounts for geometric variation aspects of the build.

The outcome of this study will pave way for many future activities. Performing a multilayer, multitrack melting simulation along with simulating the effect of build cutoff will enable capturing the effect of PSD and layer thickness at a larger scale. Also, the scope will be further expanded as per the robust design methodology where various factors will be classified into control factors and noise factors. Optimizing the control factors such as the build direction, scanning strategy, and layer thickness support structures by considering the effect of noise factors such as chemical composition and stochastic powder distribution due to the recoater system will be studied. A long-term objective is to consider these build-level effects while planning part positioning and fixture design aspects in hybrid manufacturing and postprocessing scenarios. However, to perform all the aforementioned activities, long simulation times and high cost incurred will have to be handled. Hence, faster simulation techniques will also be explored.

Acknowledgment

The work was carried out in the framework of the Centre for Additive Manufacturing—Metal (CAM²) funded by the Swedish Government Agency for Innovation Systems, VINNOVA. The support is gratefully acknowledged.

Conflict of Interest

There are no conflicts of interest.

Data Availability Statement

The datasets generated and supporting the findings of this article are obtainable from the corresponding author upon reasonable request. The authors attest that all data for this study are included in the paper.

References

- [1] Tan, J. H., Wong, W. L. E., and Dalgarno, K. W., 2017, "An Overview of Powder Granulometry on Feedstock and Part Performance in the Selective Laser Melting Process," *Addit. Manuf.*, **18**, pp. 228–255.
- [2] Gu, H., Gong, H., Dilip, J., Pal, D., Hicks, A., Doak, H., and Stucker, B., 2014, "Effects of Powder Variation on the Microstructure and Tensile Strength of Ti6Al4V Parts Fabricated by Selective Laser Melting," Proceedings of the 25th Annual International Solid Freeform Fabrication Symposium, Austin, TX, Aug. 4–6, pp. 4–6.
- [3] Strondl, A., Lyckfeldt, O., Brodin, H., and Ackelid, U., 2015, "Characterization and Control of Powder Properties for Additive Manufacturing," *JOM*, **67**(3), pp. 549–554.
- [4] Mori, S., Doi, K., Maruyama, S., Hanami, K., Kitagaki, H., Terauchi, S., and Matsushita, T., 2018, "Effect of Particle Size on the Quality Characteristics of Pure Titanium Fabricated Using Metal Additive Manufacturing," *J. Jpn. Soc. Powder Powder Metall.*, **65**(7), pp. 431–435.
- [5] Balbaa, M., Ghasemi, A., Fereiduni, E., Elbestawi, M., Jadhav, S., and Kruth, J.-P., 2021, "Role of Powder Particle Size on Laser Powder Bed Fusion Processability of AlSi10 mg Alloy," *Addit. Manuf.*, **37**, p. 101630.
- [6] Jacob, G., Jacob, G., Brown, C. U., and Donmez, A., 2018, *The Influence of Spreading Metal Powders With Different Particle Size Distributions on the Powder Bed Density in Laser-Based Powder Bed Fusion Processes*, US Department of Commerce, National Institute of Standards and Technology, Gaithersburg, MD.
- [7] Coe, H. G., and Pasebani, S., 2020, "Use of Bimodal Particle Size Distribution in Selective Laser Melting of 316 L Stainless Steel," *J. Manuf. Mater. Process.*, **4**(1), p. 8.
- [8] Lee, Y., and Zhang, W., 2016, "Modeling of Heat Transfer, Fluid Flow and Solidification Microstructure of Nickel-Base Superalloy Fabricated by Laser Powder Bed Fusion," *Addit. Manuf.*, **12**, pp. 178–188.
- [9] Rausch, A. M., Küng, V. E., Pobel, C., Markl, M., and Körner, C., 2017, "Predictive Simulation of Process Windows for Powder Bed Fusion Additive Manufacturing: Influence of the Powder Bulk Density," *Materials*, **10**(10), p. 1117.
- [10] Zhang, J., Gu, D., Yang, Y., Zhang, H., Chen, H., Dai, D., and Lin, K., 2019, "Influence of Particle Size on Laser Absorption and Scanning Track Formation Mechanisms of Pure Tungsten Powder During Selective Laser Melting," *Eng.*, **5**(4), pp. 736–745.
- [11] Letenneur, M., Kreitzberg, A., and Brailovski, V., 2019, "Optimization of Laser Powder Bed Fusion Processing Using a Combination of Melt Pool Modeling and Design of Experiment Approaches: Density Control," *J. Manuf. Mater. Process.*, **3**(1), p. 21.
- [12] Tian, Y., Yang, L., Zhao, D., Huang, Y., and Pan, J., 2020, "Numerical Analysis of Powder Bed Generation and Single Track Forming for Selective Laser Melting of ss316 L Stainless Steel," *J. Manuf. Process.*, **58**, pp. 964–974.
- [13] Dawes, J., Bowerman, R., and Trepleton, R., 2015, "Introduction to the Additive Manufacturing Powder Metallurgy Supply Chain," *Johnson Matthey Technol. Rev.*, **59**(3), pp. 243–256.
- [14] Phadke, M. S., 1995, *Quality Engineering Using Robust Design*, Prentice Hall PTR, Hoboken, NJ.
- [15] Cundall, P. A., and Strack, O. D. L., 1979, "A Discrete Numerical Model for Granular Assemblies," *Geotechnique*, **29**(1), pp. 47–65.
- [16] Gohl, J., Markstedt, K., Mark, A., Ha kansson, K., Gatenholm, P., and Edelvik, F., 2018, "Simulations of 3d Bioprinting: Predicting Bioprintability of Nanofibrillar Inks," *Biofabrication*, **10**(3), p. 034105.
- [17] Gohl, J., Mark, A., Sasic, S., and Edelvik, F., 2018, "An Immersed Boundary Based Dynamic Contact Angle Framework for Handling Complex Surfaces of Mixed Wettabilities," *Int. J. Multiphase Flow*, **109**, pp. 164–177.
- [18] Gouge, M., and Michaleris, P., 2018, *Thermo-Mechanical Modeling of Additive Manufacturing*, Butterworth-Heinemann, New York.
- [19] GKN Hoeganaes, 2020, "Ancor AM 316L," <https://www.gknpm.com/globalassets/downloads/hoeganaes/technical-library/datasheets/datasheets-for-am-materials/ancoram-steel/ancor-am-316l.pdf>, Accessed May 8, 2020.
- [20] Kim, C. S., 1975, "Thermophysical Properties of Stainless Steels," Argonne National Laboratory, IL, *Technical Report* No. ANL-75-55.
- [21] Mills, K. C., 2002, *Recommended Values of Thermophysical Properties for Selected Commercial Alloys*, Woodhead Publishing, Cambridge, UK.
- [22] Spierings, A. B., and Levy, G., 2009, "Comparison of Density of Stainless Steel 316 L Parts Produced With Selective Laser Melting Using Different Powder Grades," Proceedings of the Annual International Solid Freeform Fabrication Symposium, Austin, TX, Aug. 3–5, pp. 342–353.